REVIEW

Recent Advances in Anode Materials of Solid Oxide Electrolysis Cells

Geng Zou [a,b], Wei-Cheng Feng [a,b], Yue-Feng Song [a,*], Guo-Xiong Wang [a,*]

[a] State Key Laboratory of Catalysis, Dalian National Laboratory for Clean Energy, Dalian Institute of Chemical Physics, Chinese Academy of Sciences, Dalian, 116023, Liaoning, China
[b] University of Chinese Academy of Sciences, Beijing, 100049, China

Abstract

Solid oxide electrolysis cell (SOEC) as an electrochemical energy conversion device has attracted increasing attention due to its large current density, high Faradaic efficiency and energy efficiency. Oxygen evolution reaction at the anode, a four-electron transfer process, is an important half-reaction for SOEC, which contributes to the main polarization resistance and consumes most electric energy during the electrolysis process. Hence, designing anode materials with high activity and stability is crucial for the performance improvement and practical application of SOEC. Recently, some advances have been made in the development of high-performance anode. In the current review, the mechanisms for CO_2 and/or H_2O electrolysis are highlighted. The physicochemical and electrochemical properties of different types of anodes are summarized. Various efficient strategies for anode optimization are introduced. Furthermore, the outlook for the future research of SOEC is included. This review might be helpful for the development of anode materials and the practical application of SOEC.

Keywords: Solid oxide electrolysis cell; Anode materials; CO_2 and/or H_2O electrolysis; Perovskite oxide

1. Introduction

The development of modern industry consumes vast fossil fuels (e.g. coal, natural gas, petroleum), which not only causes serious energy crisis but also leads to notorious greenhouse effect owing to the tremendous CO_2 emission. According to the long-term monitoring by Mauna Loa Observatory, the atmospheric concentration of CO_2 grew from 5.76×10^{-4} kg·m^{-3} in 1960 to 7.69×10^{-4} kg·m^{-3} in 2020 [1]. Meanwhile, renewable energy resources (e.g. solar, wind, tide, geothermal) have been developed rapidly in recent years, however, their shortcomings such as uneven spatial and temporal distributions limit their practical application. Electroreduction of CO_2 and/or H_2O to useful chemicals/fuels powered by renewable energy could efficiently reduce the atmospheric concentration of CO_2 and simultaneously provide a stable energy storage method for renewable energy resources. Among all the electrochemical technologies, solid oxide electrolysis cell (SOEC) is considered as a promising approach due to its high current density and Faradaic efficiency, satisfactory stability and unrivaled electrolysis efficiency [2].

Typical SOEC includes porous anode, dense electrolyte and porous cathode, as shown in Fig. 1. During CO_2 and H_2O co-electrolysis, CO_2 and H_2O are electrochemically reduced to CO and H_2 at the cathode, respectively, accompanied with the reverse water-gas shift reaction, and then O^{2-} passes through the electrolyte to the anode to form O_2 (oxygen evolution reaction, OER). The electroreduction of CO_2 or H_2O at the cathode is a two-electron transfer process, while the OER reaction at the anode is a four-electron transfer process, which contributes to the main polarization

Received 2 June 2022; Received in revised form 23 June 2022; Accepted 31 August 2022
Available online 4 September 2022

* Corresponding author, Yue-Feng Song, Tel: (86-411)84379511, E-mail address: songyf2014@dicp.ac.cn.
* Corresponding author, Guo-Xiong Wang, Tel: (86-411)84379511, E-mail address: wanggx@dicp.ac.cn.

https://doi.org/10.13208/j.electrochem.2215006

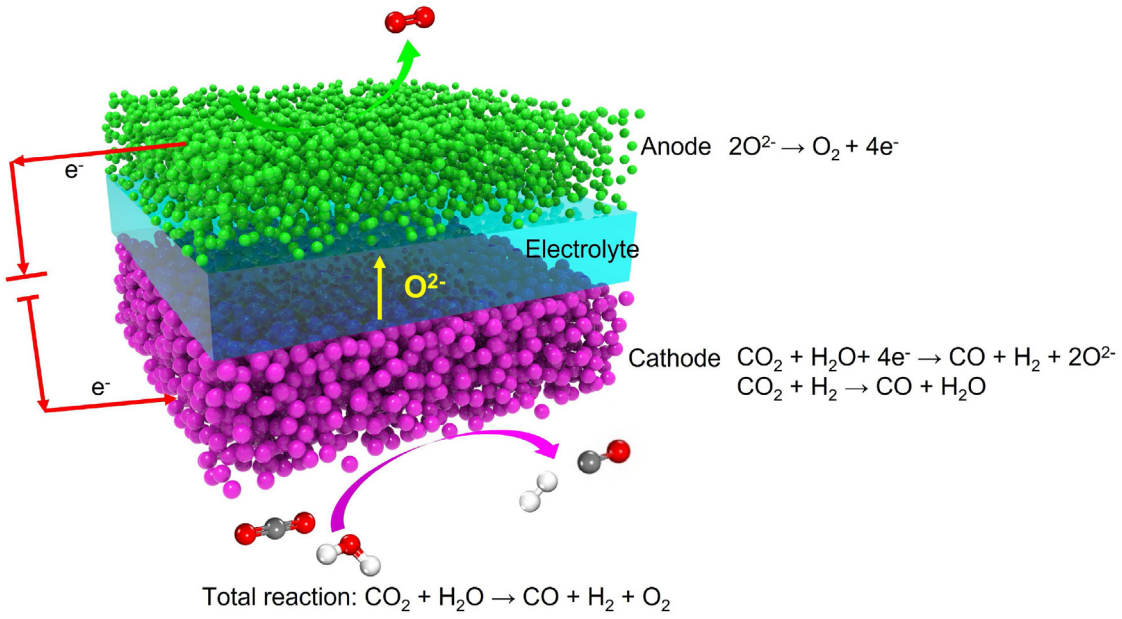

Fig. 1. Schematic of SOEC for H_2O and CO_2 co-electrolysis.

resistance (R_P) and consumes most electric energy in the electrolysis process. Hence, designing advanced anode materials is a crucial step for the performance improvement of SOEC [3,4]. Typically, a high-performance anode material should possess high mixed ionic and electronic conductivity (MIEC), satisfactory physical and electrochemical stabilities, favorable OER activity and appropriate thermal expansion coefficient (TEC) with electrolytes. However, several challenges such as ion segregation, structure failure and poor OER activity of the common anode materials limit the practical application of SOEC. Herein, the physicochemical properties and modification strategies of anode materials are summarized to provide helpful instructions for the design of efficient anode materials with high OER activity and long-term stability.

2. SOEC anode materials

Perovskite-type oxides and spinel oxides (AB_2O_4) are the common anode materials and their crystal structures are shown in Fig. 2. Perovskite-type oxides include single perovskite oxides ($ABO_{3-\delta}$), double perovskite oxides ($AA'B_2O_{5+\delta}$ and $A_2BB'O_{6-\delta}$, and Ruddlesden-Popper (RP) phase oxides ($A_{n+1}B_nO_{3n+1}$). In perovskite oxides, the A-site is usually occupied by the larger alkaline earth or rare earth metal cations (e.g. La^{3+}, Sr^{2+}, Ba^{2+}, Ca^{2+}, Bi^{3+}, Pr^{3+}, Gd^{3+}) to stabilize crystal structure, while the B-site is usually occupied by smaller transition metal ions (e.g. Mn^{3+}, Co^{3+}, Fe^{3+}, Ni^{3+}) to tune the electrocatalytic performance. In spinel oxides, the A-site is occupied by bivalent cations (e.g. Mg^{2+}, Fe^{2+}, Co^{2+}) while the B-site is occupied by trivalent cations (e.g. Al^{3+}, Fe^{3+}, Co^{3+}).

3. $ABO_{3-\delta}$ type perovskite oxides

3.1. Mn-based perovskite anodes

$La_{1-x}Sr_xMnO_{3-\delta}$ (LSM) is the most widely used SOEC anode material due to its high electronic conductivity (1.0×10^2 S·cm^{-1}, 800 °C) and compatible TEC (1.0×10^{-5}–1.1×10^{-5} K^{-1}) with Y-stabilized ZrO_2 (YSZ) electrolyte (1.0×10^{-5}–1.1×10^{-5} K^{-1}) [5,6]. The Sr^{2+} doping at the A-site of $LaMnO_{3-\delta}$ can change the valence states of Mn species and increase the electrical conductivity of $LaMnO_{3-\delta}$ [7]. Generally, the doping amount of Sr^{2+} is usually around 20%–30% because the TEC is increased and the oxygen chemical diffusion coefficient (D^*) is reduced with the Sr^{2+} content [6,8]. SOEC with LSM anode exhibited a current density of 0.80 A·cm^{-2} at 1.2 V and 850 °C for CO_2 electrolysis [9]. However, the ionic conductivity (1.0×10^{-7}–1.0×10^{-8} S·cm^{-1}, 800 °C) [5], D^* (3.2×10^{-16} cm^2·s^{-1}, 700 °C), and surface oxygen exchange coefficient (k^*) (2.0×10^{-9} cm·s^{-1}, 700 °C) of LSM are relatively low [10]. Moreover, LSM suffers from the delamination from electrolyte, which is attributed to the following reasons: (1) the lattice shrinkage of LSM and local tensile strain result in the microcrack formation at the anode/electrolyte interface [11]; (2) the diffusion of oxygen gas is limited by the pore structure in anode layer at high current densities, uplifting the oxygen partial at the anode/electrolyte interface, finally leading to the delamination of anode [12]. To improve the

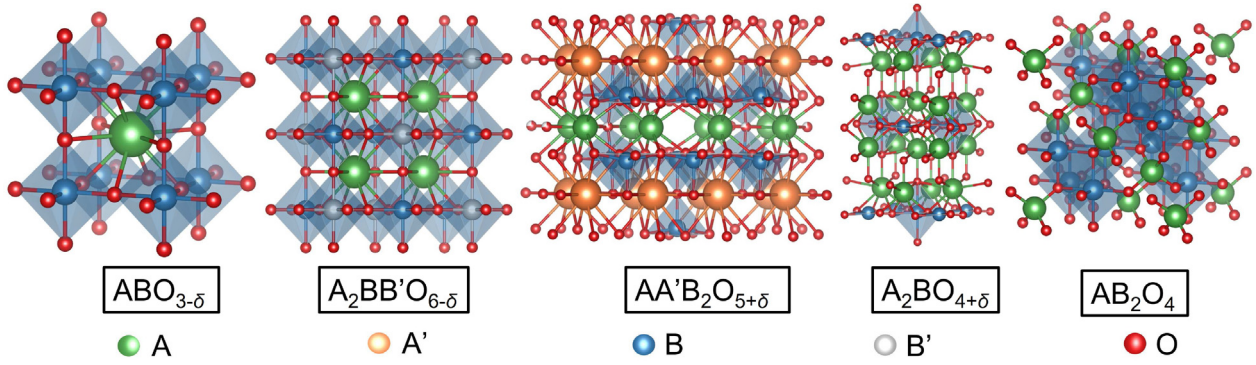

Fig. 2. Crystal structures of (from left to right) single perovskite oxides ($ABO_{3-\delta}$), double perovskite oxides ($A_2BB'O_{6-\delta}$), double perovskite oxides ($AA'B_2O_{5+\delta}$), Ruddlesden-Popper phase ($A_{n+1}B_nO_{3n+1}$, $n = 1$) and spinel (AB_2O_4).

performance and stability of LSM-based anode materials, a multitude of studies have been conducted by doping different metal cations at the A or B-site. For example, Mahata et al. substituted Sr^{2+} by smaller Ca^{2+} at the A-site of LSM and synthesized the novel $La_{0.65}Sr_yCa_{(0.3-y)}MnO_3$ (LSCaM) with a more symmetrical crystal structure, which displayed larger specific surface area, higher electrical conductivity and oxygen vacancy concentration, thus exhibiting higher OER performance and better stability than LSM [13].

3.1.1. Co-based perovskite anodes

$La_{1-x}Sr_xCoO_{3-\delta}$ (LSC) is the most common Co-based SOEC anode material, which exhibits higher ionic conductivity (2.2×10^{-1} S·cm^{-1}, 800 °C), electronic conductivity (1.6×10^{3} S·cm^{-1}, 800 °C), D^* (9.5×10^{-7} cm^2·s^{-1}, 800 °C) and k^* (7.0×10^{-6} cm·s^{-1}, 800 °C) than LSM [14,15]. The electrochemical performance of LSC-$Ce_{1-x}Gd_xO_{2-\delta}$ (GDC) anode is better than those of LSM-YSZ and $La_{1-x}Sr_xCo_{1-y}Fe_yO_{3-\delta}$ (LSCF)-GDC at 800 °C for H_2O electrolysis [16]. Though LSC exhibits excellent performance [17], it also has shortages such as the twice higher TEC (20.5×10^{-6} K^{-1}) than that of YSZ electrolyte [14] and Sr segregation [17]. Doping Ni into the B-site of LSC could reduce the TEC to 17.8×10^{-6} K^{-1} and increase the ionic conductivity [18]. Recently, Chi et al. evaluated the performance of infiltrated $La_{0.8}Sr_{0.2}Co_{0.8}Ni_{0.2}O_{3-\delta}$-GDC (LSCN-GDC) anode for H_2O electrolysis with a current density of 1.06 A·cm^{-2} at 1.0 V and 800 °C [19]. The scanning electron microscopic (SEM) images of LSCN-GDC (Fig. 3a–b) confirmed that the size of LSCN particles was less than 50 nm and the LSCN nanoparticles were uniformly distributed on the GDC framework. And the stability of LSCN-GDC anode was also improved due to the active sites expanding to the surface of GDC framework, which might avoid the delamination of the anode.

Meanwhile, $LaNi_{1-x}Co_xO_3$ (LNC) has also been employed as the SOEC anode due to its compatible TEC, high electrical conductivity and lower cost [20]. The infiltrated LNC-GDC anode with excellent adsorption/desorption ability of O_2 and high electric conductivity (Fig. 3c) exhibited favorable Faradaic efficiency (>90%) and a current density of 2.32 A·cm^{-2} at 2.0 V and 800 °C for pure CO_2 electrolysis (Fig. 3d) [21]. The anode with A-site deficient LNC displayed excellent electrochemical performance of 2.00 A·cm^{-2} at 1.2 V and 800 °C, and good long-term stability for H_2O electrolysis [22]. Additionally, other Co-based materials such as $SrCo_{0.8}Nb_{0.2}O_{3-\delta}$ (SCNb), $SrCo_{0.8}Ta_{0.2}O_{3-\delta}$ (SCT), and $SrCo_{0.8}Nb_{0.1}Ta_{0.1}O_{3-\delta}$ (SCNbT) have also been reported as anode materials [23].

3.1.2. Fe-based perovskite anodes

$La_{1-x}Sr_xFeO_{3-\delta}$ (LSF) is another commonly used anode material of SOEC due to its excellent ionic conductivity (2.0×10^{-1}–4.7×10^{-2} S·cm^{-1}, 800 °C) [24], suitable electronic conductivity (213.0 S·cm^{-1} 650 °C) [25] and proper TEC (11.7×10^{-6} K^{-1}) [26]. Han et al. investigated the electrochemical performance of LSF-YSZ for H_2O electrolysis, which exhibited a current density of 0.66 A·cm^{-2} at 1.3 V and 800 °C [27]. Several kinds of novel Fe-based anode materials have been fabricated by doping transition metal cations at the B-site of LSF such as $La_{1-x}Sr_xFe_{1-y}Nb_yO_{3-\delta}$ (LSFNb) [28], $La_{1-x}Sr_xFe_{1-y}Cr_yO_{3-\delta}$ (LSFC) [29], $La_{1-x}Sr_xFe_{1-y}Ni_yO_{3-\delta}$ (LSFN) [30], $La_{0.1}Sr_{0.85}Ti_{0.35}Fe_{0.6}Ni_{0.05}O_3$ (LSTFN) [31], and $La_{0.6}Sr_{0.4}Fe_{0.9}Mn_{0.1}O_{3-\delta}$ (LSFM) [32]. The partial substitution of Fe could greatly improve the stability and performance of SOEC. Chi et al. investigated the effect of B-site substitution on the OER activity of LSFN anode for pure CO_2 electrolysis [30]. The LSFN-GDC anode could reach a current density of 1.03 A·cm^{-2} at 2.0 V and 800 °C, but with poor stability due to the Sr segregation during the long-

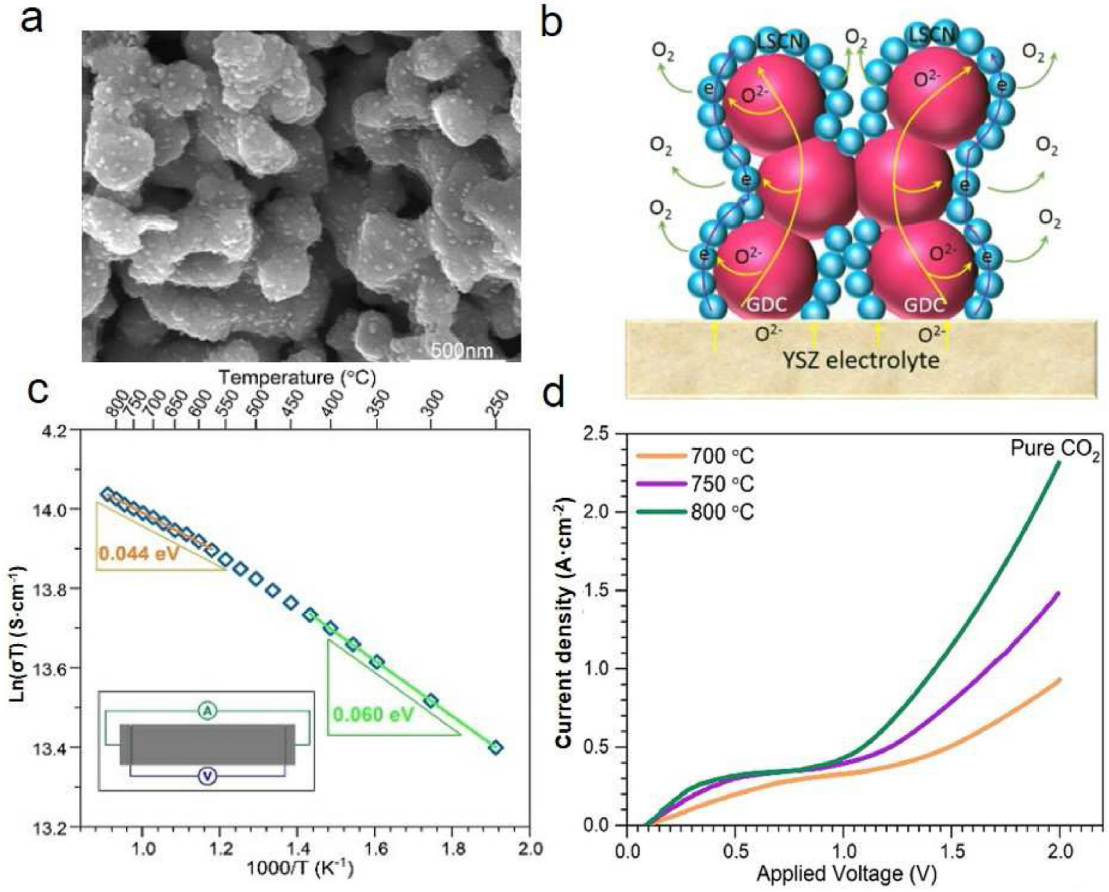

Fig. 3. (a) SEM image of the cross-section of the porous GDC scaffold infiltrated with LSCN nanoparticles. (b) Schematic diagram of the infiltrated LSCN-GDC anode. Reproduced with permission of Ref. [19], copyright 2016 Elsevier. (c) The conductivity of LCN samples measured by direct current four-probe method. (d) Current density-voltage (J−V) curves of SOEC with LCN-GDC anode for pure CO_2 electrolysis. Reproduced with permission of Ref. [21], copyright 2022 Elsevier.

term operation at high temperatures. However, the Sr segregation phenomenon could be inhibited by applying LSFN anode in the reversible solid oxide cell, and the cell showed a higher current density of 1.09 $A \cdot cm^{-2}$ at 1.3 V and 800 °C with improved stability [33]. In addition, doping Mn at the B-site of LSF (LSFM) could increase the oxygen vacancy concentration and promote the electrochemical performance, delivering a current density of 1.74 $A \cdot cm^{-2}$ at 2.0 V and 850 °C for pure CO_2 electrolysis [32].

Besides, other Fe-based perovskite oxides such as $Bi_{1-x}Sr_xFe_{1-y}Ta_yO_{3-\delta}$ (BSFTa) [34], $La_{1-x}Ca_xFeO_{3-\delta}$ (LCF) [35], and $La_{1-x}Ca_xFe_{1-y}Ni_yO_{3-\delta}$ (LCFN) [36] have also been used as anode materials. The BSFTa anode showed proper TEC of 12.3 × 10^{-6} K^{-1} (Fig. 4a) and good thermal compatibility with electrolytes [34]. The electrochemical impedance spectroscopic (EIS) (Fig. 4b and d), distribution of relaxation time (DRT) analyses (Fig. 4c) and R_P of the high and low frequency arcs with increased Ta concentration (Fig. 4e) indicated the Ta doping could increase the oxygen vacancy concentration and facilitate OER kinetics. Therefore, BSFTa exhibited higher electrochemical performance than $Bi_{1-x}Sr_xFe_1O_{3-\delta}$ (BSF) as shown in Fig. 4f and g. Ca-doped Fe-based perovskite oxide showed increased electrical conductivity, oxygen vacancy concentration and D^* and k^* [35]. LCFN-GDC anode displayed a maximum current density of 1.41 $A \cdot cm^{-2}$ at 2.0 V and 800 °C for pure CO_2 electrolysis [36].

3.1.3. Co and Fe co-doped perovskite anodes

The Co and Fe co-doped perovskite oxides show high oxygen vacancy concentration and variable valence from +2 to +4 of transition metal cations at the B-site, which is conducive to promoting the transport of oxygen ions and the exchange of oxygen species on the surface. $La_{1-x}Sr_xCo_{1-y}Fe_yO_{3-\delta}$ (LSCF) and $Ba_{1-x}Sr_xCo_{1-y}Fe_yO_{3-\delta}$ (BSCF) are the two most common Co and Fe co-doped perovskite anodes for SOEC [37,38]. LSCF shows high electronic conductivity (57.0 $S \cdot cm^{-1}$ at 600 °C) [39], D^* (5.0 × 10^{-7} $cm^2 \cdot s^{-1}$, 900 °C) and k^* (4.0 × 10^{-5} $cm \cdot s^{-1}$, 900 °C) [40], and thus exhibits higher electrochemical performance than LSM

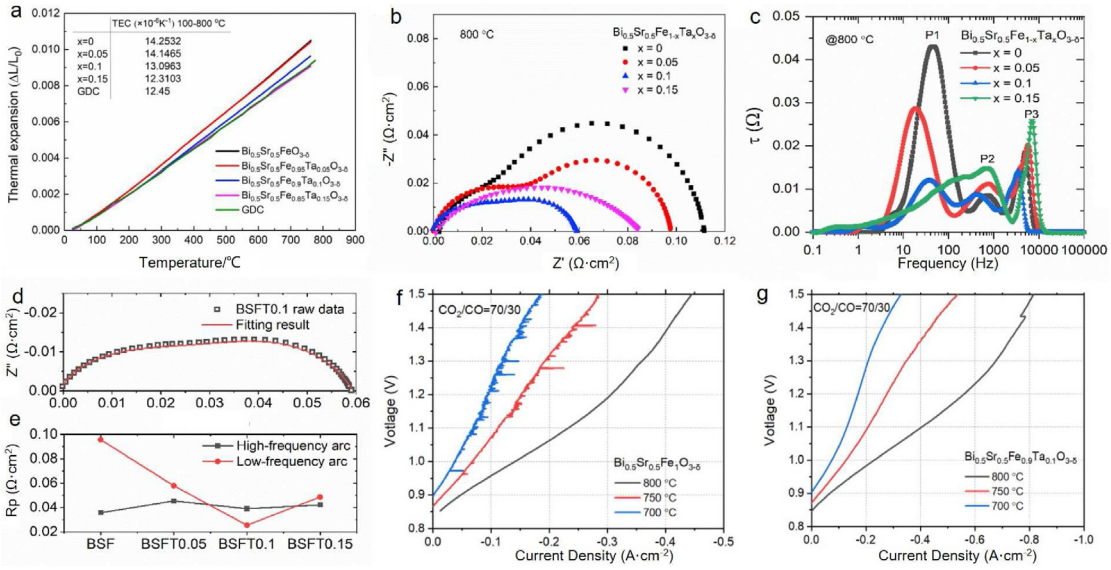

Fig. 4. (a) TEC of Ta-doped BSF anodes with different Ta doping amounts from room temperature to 750 °C. (b) Electrochemical impedance spectroscopic (EIS) plots of BSFTa anode with different Ta doping amounts at 800 °C. (c) Distribution function of relaxation time analysis of BSFTa at 800 °C. (d) Sample equivalent fitting of BSFTa. (e) Variation in R_P of the high and low-frequency arcs of BSFTa at 800 °C. J-V curves of (f) BSF and (g) BSFTa anodes for CO_2 electrolysis at different temperatures. Reproduced with permission of Ref. [34], copyright 2022 Elsevier.

anode [41]. Hence, LSCF is a potential anode material for SOEC, but it also has such shortages as low ionic conductivity (2.6×10^{-4} S·cm^{-1}, 800 °C) [42] and incompatible TEC (17.5×10^{-6} K^{-1}) with electrolytes [43]. Recently, Jiang et al. found that the directly assembled LSCF anode onto the YSZ electrolyte at low temperatures could effectively suppress the Sr segregation and improve the current density to 1.50 A·cm^{-2} at 1.26 V and 750 °C for H_2O electrolysis [44]. Additionally, doping high-valance metal cations at the B-site of LSCF could improve the stability of the electrode materials. Yang et al. fabricated Nb-doped LSCF ($La_{0.4}Sr_{0.6}Co_{0.2}Fe_{0.7}Nb_{0.1}O_{3-\delta}$, LSCFNb), which delivered a current density of 0.64 A·cm^{-2} at 1.3 V and 850 °C for CO_2 and H_2O co-electrolysis with lower degradation rate [45].

BSCF is firstly applied as the oxygen permeable membrane [46] due to its higher oxygen ionic conductivity (1.9 S·cm^{-1}, 900 °C) [47], D^* (8.0×10^{-7} cm^2·s^{-1}, 800 °C) [48] and k^* (5.0×10^{-5} cm·s^{-1}, 750 °C) [49] than LSM and LSCF [50]. Therefore, BSCF is a promising anode material of SOEC and exhibits higher electrochemical performance than LSM for H_2O electrolysis. However, BSCF still has some problems such as structural instability, and higher TEC (19.7×10^{-6} K^{-1}) than that of most electrolytes [51]. Luo et al. prepared $La_{0.5}Ba_{0.25}Sr_{0.25}Co_{0.8}Fe_{0.2}O_{3-\delta}$ with fibrous, porous structure to inhibit the phase transformation from cubic to hexagonal phase by doping La^{3+} at the A-site, thus improving the electrochemical performance and stability of SOEC [52]. Additionally, doping Ta^{5+} at the B-site made a compromise between the MIEC and stability of the anode, and the $Ba_{0.5}Sr_{0.5}(Co_{0.8}Fe_{0.2})_{1-x}Ta_xO_{3-\delta}$ (BSCFTa) delivered a current density of 1.06 A·cm^{-2} at 1.5 V and 800 °C [53].

Aside from LSCF and BSCF, $Ba_{0.9}Co_{0.5}Fe_{0.4}Nb_{0.1}O_{3-\delta}$ (BCFNb) has also been examined for H_2O electrolysis. Chen et al. studied the electrochemical performance of SOEC with BCFNb as anode for H_2O electrolysis, which exhibited an excellent performance of 3.24 A·cm^{-2} at 1.5 V and 850 °C, and low R_P of 0.08 Ω·cm^2 at 750 °C [54].

3.2. Double perovskite anodes

$Sr_2Fe_{2-y}Mo_yO_{6-\delta}$ (SFM) is the most common double perovskite for anode materials due to its suitable electronic conductivity (20.9 S·cm^{-1}, 600 °C), D^* (9.0×10^{-6} cm^2·s^{-1}, 800 °C) and k^* (8.0×10^{-5} cm·s^{-1}, 800 °C) [55,56]. SFM, as a symmetrical SOEC electrode, exhibited a current density of 0.88 A·cm^{-2} at 1.3 V and 900 °C for H_2O electrolysis [57]. But SFM shows low ionic conductivity (2.1×10^{-4} S·cm^{-1}, 800 °C) [55] and high TEC (14.9×10^{-6}–18.6×10^{-6} K^{-1}) [58]. The incorporation of Co into the B-site of SFM can enhance the catalytic activity and conductivity. Recently, $Sr_2Fe_{1.3}Co_{0.2}Mo_{0.5}O_{6-\delta}$ (SFCM) was used as the symmetrical electrodes of SOEC, which exhibited a current density of 2.30 A·cm^{-2} at 1.5 V and 800 °C for CO_2 and H_2O co-electrolysis, and good stability for 20 h at 0.40 A·cm^{-2} and 800 °C [59]. Moreover, the optimization of A-site could

also improve the activity of the anode. By doping K^+ with higher basicity and larger ionic radius to the A site, the oxygen vacancy formation energy is reduced, and the reaction kinetics is improved, thus enhancing the electrochemical performance of the anode by 93.4% at 600 °C [60].

Apart from SFM, $Ln_{2-x}Ba_xCo_2O_{5+\delta}$ (Ln = Gd, Nd, Sm, Pr) double perovskite oxides are other common anode materials due to their high electrical conductivity, D^* and k^* (Table 1). Jiang et al. proposed $SmBaCo_2O_{5+\delta}$ as an anode material with R_P as low as 0.024 Ω·cm^2 at 900 °C [61]. Zheng et al. employed Ca and Fe co-doped SBC ($SmBa_{0.75}Ca_{0.25}CoFeO_{5+\delta}$, SBCCF) as an anode, which showed higher phase stability than SBC under the electrolysis current of 1.00 A·cm^{-2} at 800 °C for 216 h [62].

Additionally, other double perovskite oxides with remarkable OER activities and stabilities also have been reported, such as $Sr_2Ti_{1-y}Co_yFeO_{6-\delta}$ (STCF) [63], $PrBaMn_2O_{5+\delta}$ (PBM) and $PrBa_{0.5}Sr_{0.5}Co_{1.5}Fe_{0.5}O_{5+\delta}$ (PBSCF) [64,65].

3.3. RP phase anodes

$Ln_2NiO_{4+\delta}$ (Ln = Nd, La, Pr) exhibits a layered structure with the alternate distribution of monolayer LnO and $LnNiO_3$, which allows it to accommodate more oxygen than stoichiometry. The unique oxygen transport mechanism could accelerate oxygen mobility. Due to the large D^*, k^* and matched TEC with electrolytes [66], RP oxide is considered as a promising anode for SOEC [67]. The current densities of $Nd_2NiO_{4+\delta}$ (NNO) anode were 1.7, 3.0, and 4.2 times higher than those of LSM anode for H_2O electrolysis at 850, 800, and 750 °C, respectively [67]. Chauveau et al. compared the performances of $La_2NiO_{4+\delta}$ (LNO), NNO, and LSM anodes, and found that LNO exhibited the lowest R_P and highest current density [68]. Besides, LNO showed higher electrochemical performance and better stability than LSCF anode due to its superior oxygen surface exchange kinetics [69]. But degradation phenomenon still exists in LNO anode due to the formation of new phases or structure failure after long-term operation [69]. Furthermore, novel anode materials such as $La_2Ni_{1-x}Co_xO_{4+\delta}$ (LNCO) [70], $La_{2-x}Pr_xNiO_{4+\delta}$ (LPN) [66] and $La_{2-x}Sr_xCo_{1-y}Ni_yO_{4\pm\delta}$ (LSCNi) [71] are prepared by doping at the A-site or B-site to improve the stability of RP oxides. Bassat et al. reported the LNCO anode with higher MIEC and more interstitial oxygen than LNO anode after doping Co at the B-site, and thus showed a higher current density of 1.60 A·cm^{-2} at 1.5 V and 800 °C (Fig. 5a), and better stability (Fig. 5b) than LNO anode [70]. The $Pr_2NiO_{4+\delta}$ (PNO) anode showed superior electrochemical performance to LNO and NNO [72]. To further improve the electrochemical performance of PNO, Co-doped PNO ($Pr_2Ni_{1-x}Co_xO_{4+\delta}$, PNC) was exploited as an anode and the PNC-GDC exhibited a higher current density of 1.90 A·cm^{-2} at 1.5 V and 800 °C (Fig. 5c) for H_2O electrolysis and lower degradation rate than PNO and LSCF anodes (Fig. 5d) [73]. Moreover, other RP phase anodes have also been used in CO_2 electrolysis such as $SrEu_2Fe_2O_{7-\delta}$ (SEF) [74], Mn-doped $La_{1.5}Sr_{0.5}NiO_{4+\delta}$ ($La_{1.5}Sr_{0.5}Ni_{1-x}Mn_xO_{4+\delta}$, LSNM) [75]. Xia et al. investigated the electrochemical performance of SEF as a symmetrical electrode, which showed a current density of 1.27 A·cm^{-2} at 1.5 V and 800 °C [74].

In order to better design perovskite-type anode material, some representative anode materials' basic properties such as electrical conductivity, ionic conductivity, D^*, k^*, and TEC are summarized in Table 1.

Table 1. Physicochemical properties of perovskite-type anode materials.

Material	Electrical conductivity (S·cm^{-1})	Ionic conductivity (S·cm^{-1})	D^* (cm^2·s^{-1})	k^* (cm·s^{-1})	TEC (K^{-1})
LSM [5,6,10]	1.0×10^2 (800 °C)	1.0×10^{-7}–1.0×10^{-8} (800 °C)	3.2×10^{-16} (700 °C)	2.0×10^{-9} (700 °C)	ca. 10.0×10^{-6}
LSC [14,15]	1.6×10^3 (800 °C)	2.2×10^{-1} (800 °C)	9.5×10^{-7} (800 °C)	7.0×10^{-6} (800 °C)	20.5×10^{-6}
LSF [24–26]	213.0 (650 °C)	0.2×10^{-2}-4.7×10^{-2} (800 °C)	–	–	11.7×10^{-6}
LSCF [39,40,42,43]	57.0 (600 °C)	2.6×10^{-4} (800 °C)	5.0×10^{-7} (900 °C)	4.0×10^{-5} (900 °C)	17.5×10^{-6}
BSCF [47–49,51]	–	1.9 (900 °C)	8.0×10^{-7} (800 °C)	5.0×10^{-5} (750 °C)	19.7×10^{-6}
SFM [55,56,58]	20.9 (600 °C)	2.1×10^{-4} (800 °C)	9.0×10^{-6} (800 °C)	8.0×10^{-5} (800 °C)	ca. 16.0×10^{-6}
PBC [76,77]	645.0 (600 °C)	–	ca. 1.0×10^{-5} (350 °C)	ca. 1.0×10^{-3} (350 °C)	21.8×10^{-6}
GBC [76,77]	318.0 (600 °C)	–	3.0×10^{-7} (350 °C)	2.0×10^{-6} (350 °C)	19.3×10^{-6}
NBC [76,78]	308.0 (600 °C)	–	3.5×10^{-5} (700 °C)	ca. 3.0×10^{-4} (700 °C)	20.0×10^{-6}
SBC [77,79]	815.0–434.0 (500–800 °C)	–	2.8×10^{-6} (700 °C)	1.9×10^{-3} (700 °C)	–

Notes: $La_{1-x}Sr_xMnO_{3-\delta}$ (LSM); $La_{1-x}Sr_xCoO_{3-\delta}$ (LSC); $La_{1-x}Sr_xFeO_{3-\delta}$ (LSF); $La_{1-x}Sr_xCo_{1-y}Fe_yO_{3-\delta}$ (LSCF); $Ba_{1-x}Sr_xCo_{1-y}Fe_yO_{3-\delta}$ (BSCF); $Sr_2Fe_{2-y}Mo_yO_{6-\delta}$ (SFM); $Pr_{2-x}Ba_xCo_2O_{5+\delta}$ (PBC); $Gd_{2-x}Ba_xCo_2O_{5+\delta}$ (GBC); $Nd_{2-x}Ba_xCo_2O_{5+\delta}$ (NBC); $Sm_{2-x}Ba_xCo_2O_{5+\delta}$ (SBC).

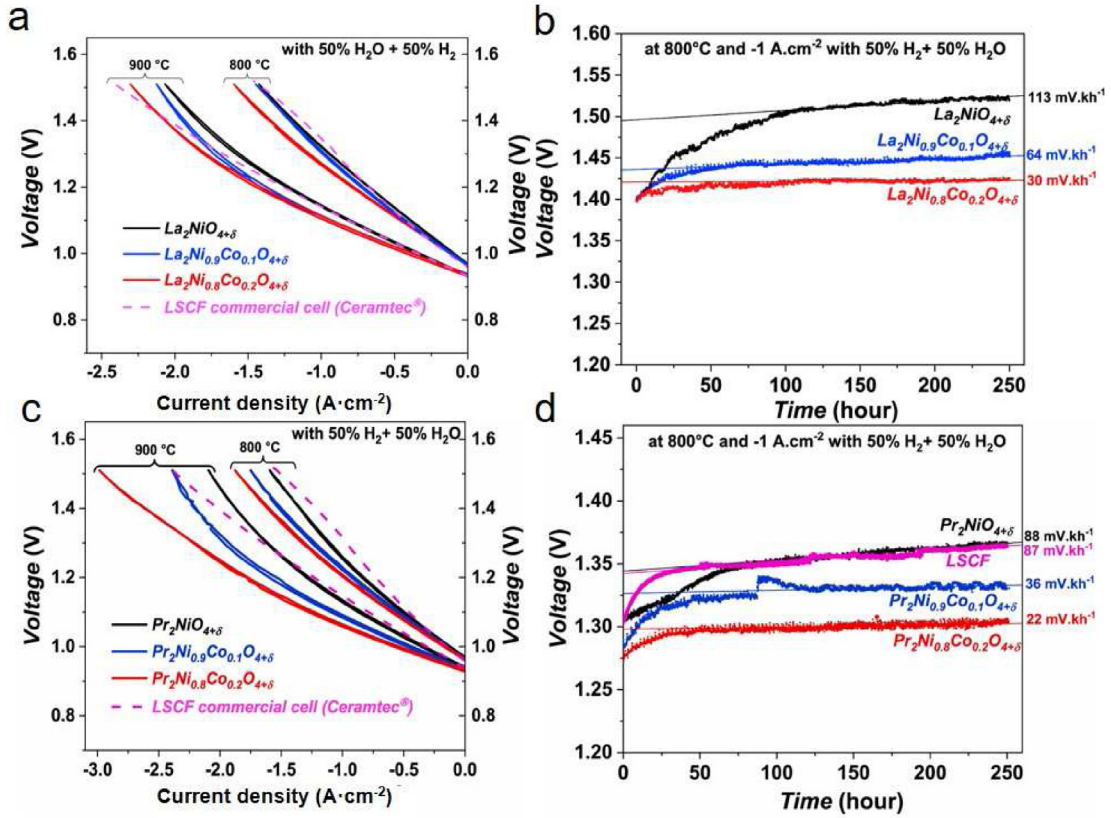

Fig. 5. (a) J-V curves for LNO, $La_2Ni_{0.9}Co_{0.1}O_{4+\delta}$ (LNCO10), $La_2Ni_{0.8}Co_{0.2}O_{4+\delta}$ (LNCO20) and LSCF anodes at 800 °C and 900 °C. (b) Stability tests of LNO, LNCO10 and LNCO20 anodes. Reproduced with permission of Ref. [70], copyright 2019 Elsevier. (c) J-V curves for PNO, PNCO10, PNCO20 and LSCF anodes at 800 °C and 900 °C. (d) Stability tests of PNO, $Pr_2Ni_{0.9}Co_{0.1}O_{4+\delta}$ (PNCO10), $Pr_2Ni_{0.8}Co_{0.2}O_{4+\delta}$ (PNCO20) and LSCF anodes. Reproduced with permission of Ref. [73], copyright 2021 Elsevier.

3.4. Spinel anodes

Spinel has drawn intense attention due to the absence of alkaline metal elements, which can efficiently suppress segregation phenomenon and side reactions with electrolytes. Chi et al. fabricated $MnCo_2O_4$-GDC as symmetrical SOEC electrodes by infiltration for pure CO_2 electrolysis, and reported that the $MnCo_2O_4$ nanoparticles were distributed on the porous GDC framework surface and exhibited a current density of 0.75 $A \cdot cm^{-2}$ at 1.5 V and 800 °C and stability of 80 h [80]. Recently, $Ni(Mn_{1/3}Cr_{2/3})_2O_4$ (NMC)-GDC composites were used as symmetrical SOEC electrodes for CO_2 electrolysis, and the cell could achieve excellent electrochemical performance (2.32 $A \cdot cm^{-2}$, 2 V, 850 °C) and high Faradaic efficiency, but the stability of NMC-GDC anode was poorer than $MnCo_2O_4$-GDC [81]. Lee et al. evaluated the performance of $CoFe_2O_4$−$Er_{0.4}Bi_{1.6}O_3$ (CFO-ESB) bifunctional anode for reversible solid oxide cells, which possessed an outstanding electrochemical performance of 1.50 $A \cdot cm^{-2}$ at 1.3 V and 700 °C [82]. However, the ionic conductivities of spinels at high temperatures are lower than those of perovskites and the stabilities under working conditions of spinels are also unsatisfactory, both limiting the application of the spinel as anode materials for SOEC [83].

Among all the introduced materials, perovskites are the most commonly used SOEC anodes due to their high mixed conductivity, relatively high OER activities and matched TEC with electrolytes. The electrochemical performances of SOEC with some representative anode materials are summarized in Table 2. However, there are still several shortcomings of the perovskites. The strengths and weaknesses of each kind of anode material are summarized in Table 3.

4. Strategies for SOEC anode optimization

4.1. Material optimization

4.1.1. Combining with ionic conductor

Most anode materials have high electronic conductivity but poor ionic conductivity, therefore, ionic conductors such as YSZ, GDC, $Ce_{1-x}Sm_xO_{2-\delta}$ (SDC) and Sc-stabilized ZrO_2 (SSZ) are normally added to the common anodes to increase the MIEC. For instance, the OER activity of LSM was enhanced

significantly after mixing with YSZ by mechanical ball milling [91]. However, composite anodes synthesized by traditional physical mixing exist some problems such as large particles, few triple-phase boundaries (TPBs) or two-phase boundaries (2 PBs) and layer delamination [91]. Recently, novel ionic conductors such as $Er_xBi_{1-x}O_{3-\delta}$ (ESB), Dy and Y co-doped Bi_2O_3 (DYSB) and Y-stabilized Bi_2O_3 (YSB) have been reported [87]. The preparation methods of electrode materials have an important impact on the electrochemical performances. Chi et al. collected the composite anodes electrochemical performances of LSM/ESB (co-synthesis) and LSM-ESB (mechanically mixing), in which the LSM/ESB showed a higher current density of 1.43 $A \cdot cm^{-2}$ at 1.5 V and 750 °C for H_2O electrolysis (Fig. 6a) due to the higher Brunauer-Emmett-Teller (BET) surface area (Fig. 6b) and electrical conductivity (Fig. 6c) of LSM/ESB compared with LSM-ESB. And the EIS curve also indicated that LSM/ESB had better SOEC performance (Fig. 6d) [92].

4.1.2. Infiltrating OER active species

Infiltration could construct a composite electrode with active nanoparticles distributed on the anode surface to increase the TPBs, and simultaneously avert the high-temperature-induced coarsening of the electrode materials, thus promoting the OER performance and stability [84]. For example, the LSM-GDC anode prepared by infiltrating GDC nanoparticles onto LSM surface [93] or infiltrating LSM nanoparticles onto GDC surface [94] could

Table 2. Electrochemical performances of SOEC with different anode materials.

Anode	Cathode	Fed gas	Current density ($A \cdot cm^{-2}$)
LSM-YSZ [84]	Ni-YSZ	80% H_2O-20% H_2	0.85@1.3 V
RuO_2+LSM-YSZ [85]	Ni-YSZ	95% CO_2–5% N_2	0.74@1.2 V
Au + LSM-YSZ [3]	Ni-YSZ	95% CO_2–5% N_2	0.94@1.4 V
STFC + LSM-YSZ [86]	Ni-YSZ	50% H_2O-50% H_2	2.00@1.3 V
LSCN + LSM-GDC [19]	Ni-YSZ	42.8% H_2O-14.4% H_2-42.8% CO_2	1.16@1.3 V
LSM-DYSB [87]	Ni-YSZ	50% H_2O-50% H_2	1.32@1.3 V
LSC-GDC [16]	Ni-YSZ	90% H_2O-10% H_2	0.60@1.1 V
LNC-GDC [21]	LNC-GDC	Pure CO_2	2.32@2.0 V
LNC-GDC [22]	Ni-YSZ	50% H_2O-50% H_2	2.00@1.2 V
LSF-YSZ [27]	Ni-YSZ	50% H_2O-25% H_2–25% N_2	0.66@1.3 V
LSF-GDC [88]	Ni-YSZ	50% CO_2–50% H_2%	2.50@1.9 V
Pt-LSF-GDC [88]	Ni-YSZ	50% CO_2–50% H_2%	3.50@1.9 V
LSFNb [28]	Ni-YSZ	50% H_2O-50% H_2	0.89@1.3 V
LSFN-GDC [30]	LSFN-GDC	Pure CO_2	1.09@1.3 V
LSFM-GDC [32]	LSFM-GDC	Pure CO_2	1.11@2.0 V
BSFTa [34]	Ni-YSZ	70% CO_2–30% CO	0.81@1.5 V
BSF [34]	Ni-YSZ	70% CO_2–30% CO	0.45@1.5 V
LCFN-GDC [36]	LCFN-GDC	Pure CO_2	1.41@2.0 V
LSCF-GDC [16]	Ni-YSZ	90% H_2O-10% H_2	0.60@1.3 V
BSCFTa [53]	Ni-YSZ	70% H_2O-30% H_2	1.06@1.5 V
RuO_2-LBSCF [52]	Ni-YSZ	70% CO_2–30% CO	1.40@1.3 V
BCFNb [54]	Ni-GDC	40% H_2O-60% H_2	3.24@1.5 V
SFM [57]	SFM	40% H_2O-60% H_2	0.88@1.3 V
Ni-SFM-SDC [89]	SFM-SDC	74% H_2–26% H_2O	1.02@0.5 V
SFM-SDC [89]	SFM-SDC	74% H_2–26% H_2O	0.34@0.5 V
Ru-SFM-SDC [90]	SFM-SDC	74% H_2–26% H_2O	1.06@0.6 V
LNO [70]	Ni-YSZ	50% H_2–50% H_2O	1.42@1.5 V
LNCO [70]	Ni-YSZ	50% H_2–50% H_2O	1.60@1.5 V

Notes: $La_{1-x}Sr_xMnO_{3-\delta}$ (LSM); Y-stabilized ZrO_2 (YSZ); $SrTi_{0.3}Fe_{0.6}Co_{0.1}O_{3-\delta}$ (STFC); $La_{0.8}Sr_{0.2}Co_{0.8}Ni_{0.2}O_{3-\delta}$ (LSCN); $Ce_{1-x}Gd_xO_{2-\delta}$ (GDC); Dy and Y co-doped Bi_2O_3 (DYSB); $La_{1-x}Sr_xCoO_{3-\delta}$ (LSC); $La_xNi_{1-x}Co_xO_3$ (LNC); $La_{1-x}Sr_xFeO_{3-\delta}$ (LSF); $La_{1-x}Sr_xFe_{1-y}Nb_yO_{3-\delta}$ (LSFNb); $La_{1-x}Sr_xFe_{1-y}Ni_yO_{3-\delta}$ (LSFN); $La_{0.6}Sr_{0.4}Fe_{0.9}Mn_{0.1}O_{3-\delta}$ (LSFM); $Bi_{1-x}Sr_xFe_{1-y}Ta_yO_{3-\delta}$ (BSFTa); $Bi_{1-x}Sr_xFe_1O_{3-\delta}$ (BSF); $La_{1-x}Ca_xFe_{1-y}Ni_yO_{3-\delta}$ (LCFN); $La_{1-x}Sr_xCo_{1-y}Fe_yO_{3-\delta}$ (LSCF); $Ba_{0.5}Sr_{0.5}(Co_{0.8}Fe_{0.2})_{1-x}Ta_xO_{3-\delta}$ (BSCFTa); $La_{0.5}Ba_{0.25}Sr_{0.25}Co_{0.8}Fe_{0.2}O_{3-\delta}$ (LBSCF); $Ba_{0.9}Co_{0.5}Fe_{0.4}Nb_{0.1}O_{3-\delta}$ (BCFNb); $Sr_2Fe_{2-y}Mo_yO_{6-\delta}$ (SFM); $La_2NiO_{4+\delta}$ (LNO); $La_2Ni_{1-x}Co_xO_{4+\delta}$ (LNCO).

Table 3. The advantages and disadvantages of each kind of anode materials.

Material	Advantage	Disadvantage
$ABO_{3-\delta}$-type perovskite oxides	High electronic conductivity	Sr segregation, low ionic conductivity
Double perovskites	Large D^* and k^*	Poor stability
RP phase oxides	Large D^*, k^*, matched TEC with electrolytes, and high OER activities	Poor stability
Spinel oxides	Suppressed Sr segregation	Poor stability and low ionic conductivity

effectively inhibit the delamination of the anode layer and improve the OER activity [93]. Wang et al. successfully prepared RuO_2 infiltrated LSM-YSZ anode, which exhibited a high current density of 0.74 $A \cdot cm^{-2}$ at 1.2 V and 800 °C for CO_2 electrolysis with lower R_P due to the newly-generated TPBs and active phase (La,Sr)$RuO_{3-\delta}$ [85] (Fig. 7a–b). And RuO_2 infiltrated $La_{0.5}Ba_{0.25}Sr_{0.25}Co_{0.8}Fe_{0.2}O_{3-\delta}$ (LBSCF) nanofiber could facilitate the OER kinetics by reducing the solid-state charge-transfer energy and enhancing the mass transportation process, and the current density reached 2.26 $A \cdot cm^{-2}$ at 1.6 V and 600 °C for CO_2 electrolysis [52] (Fig. 7c–d). Moreover, the infiltration of other metals/oxides such as Au [3], Pd [95], PdO/ZrO_2 [96], CuO [97], Ni [89], Ru/RuO_2 [90] can also improve OER catalytic activities. Additionally, perovskite oxides such as $SrTi_{0.3}Fe_{0.6}Co_{0.1}O_{3-\delta}$ (STFC) [86] and $Pr_2Ni_{1-x}Cu_xO_{4+\delta}$ [98] can be infiltrated to the anode. Zhang et al. studied the performance and stability of the SOEC with STFC-infiltrated LSM-YSZ as an anode, which exhibited a satisfactory performance and low R_P of about 0.13 $\Omega \cdot cm^2$ at 750 °C [86]. The results showed that the increase of the current density could be attributed to the higher catalytic activity of STFC than that of LSM-YSZ and the extended active sites on the surface of the electrode.

4.2. Structural optimization

As the oxygen gas diffusion kinetics is closely related to the porosity and tortuosity of the anode, the optimization of anode structure is of great importance for SOEC performance. For the coral-structured LSCF-GDC anode [99], the introduction of graphite can increase the interface porosity and TPB density, and reduce the oxygen partial pressure at the electrolyte/barrier/anode interface, which could boost the SOEC performance and stability.

Recently, Chen et al. demonstrated that the honeycomb LSC-YSZ anode (Fig. 8) possessed extremely low R_P (0.0094 $\Omega \cdot cm^2$) and excellent

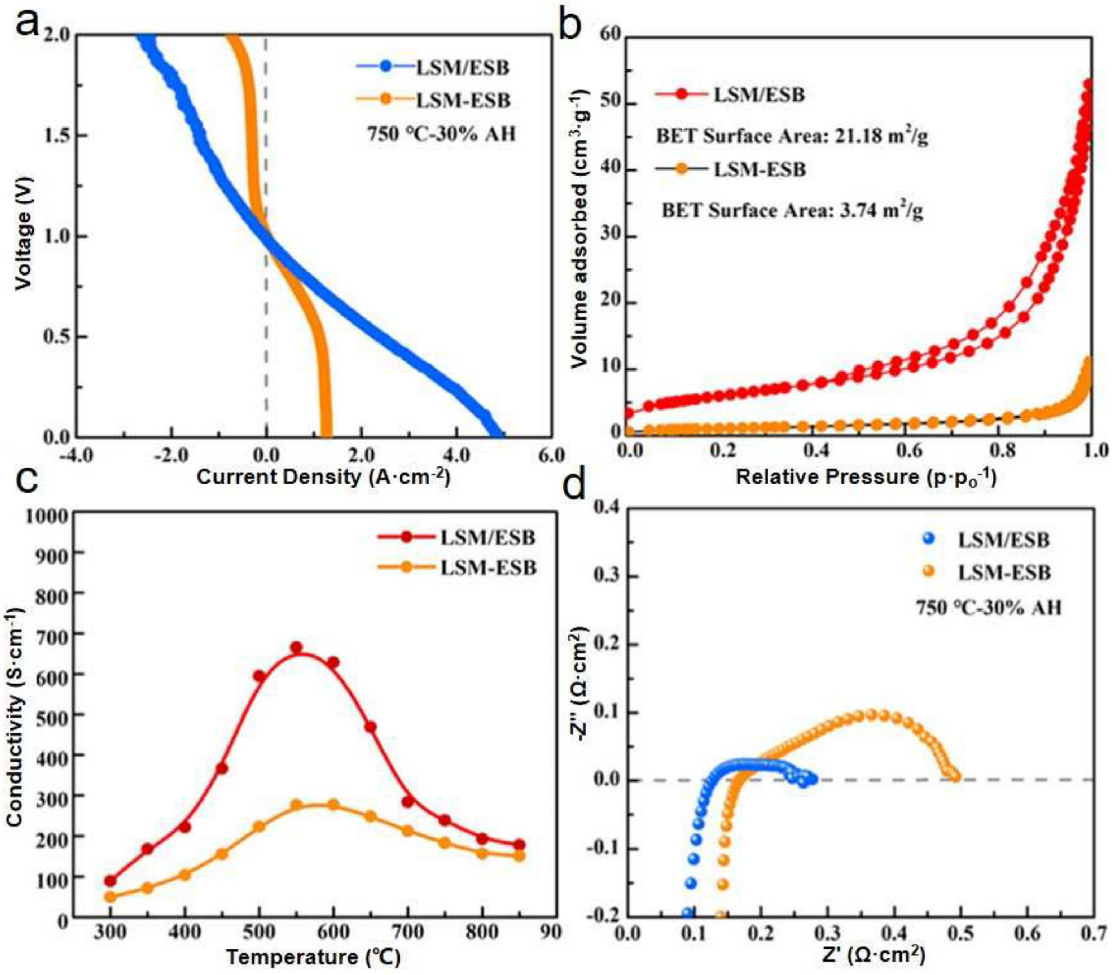

Fig. 6. Comparison of the physical chemistry properties and electrochemical performances of LSM/ESB and LSM-ESB. I–V (a), BET (b), electrical conductivity in the air (c), and EIS curves (d). Reproduced with permission of Ref. [92], copyright 2020 American Chemical Society.

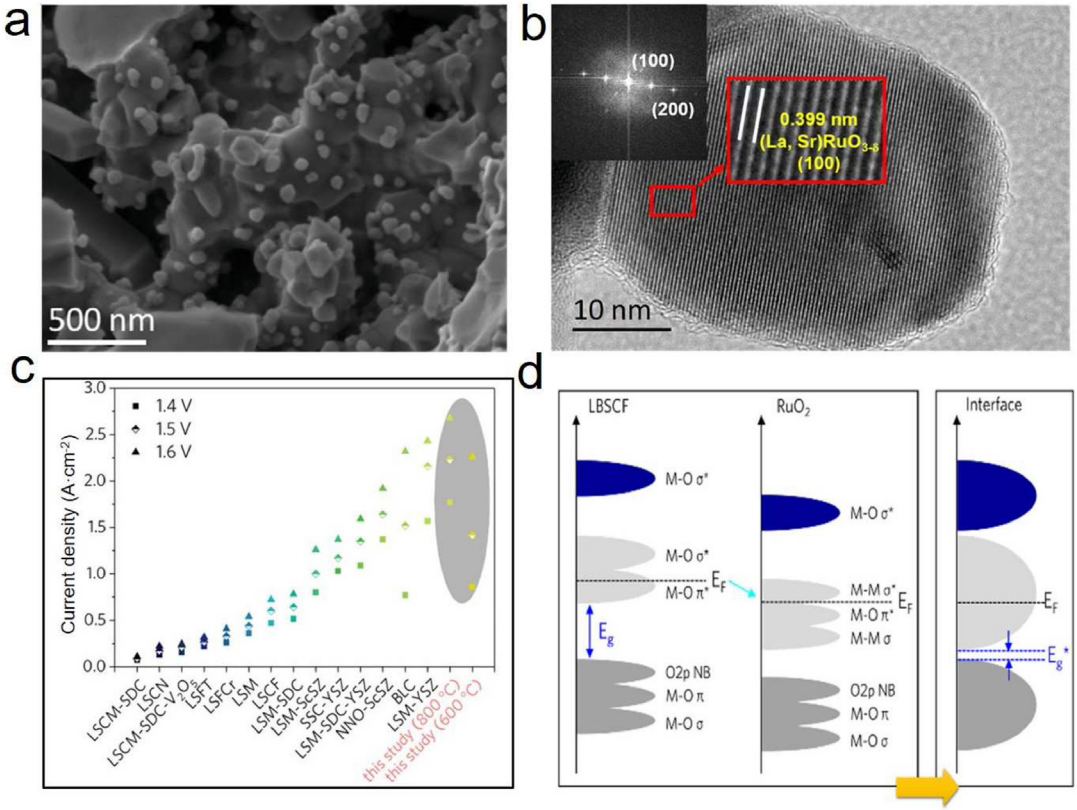

Fig. 7. (a) SEM image and (b) High-resolution transmission electron microscopic (HRTEM) image of RuO_2 infiltrated LSM-YSZ anode. Reproduced with permission of Ref. [85], copyright 2018 Elsevier. (c) Comparison of the current densities of the state-of-the-art SOEC for CO_2 electrolysis at 800 °C. (d) Schematic rigid band diagrams before and after the formation of RuO_2/LBSCF interface. Reproduced with permission of Ref. [52], copyright 2019 Elsevier.

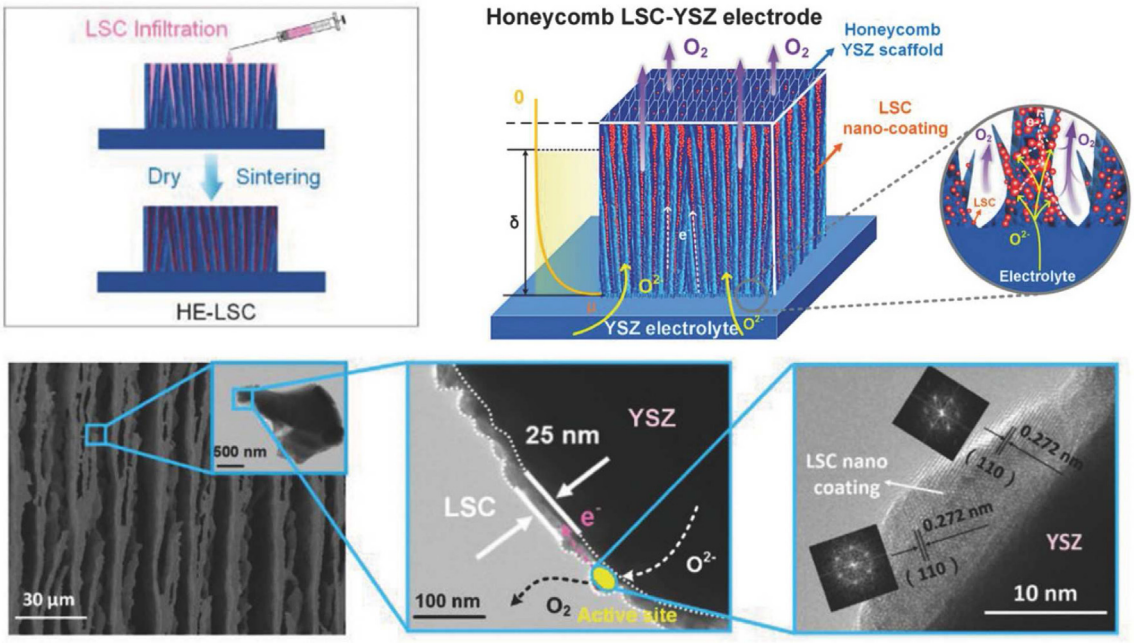

Fig. 8. Structures of LSC nanoparticles on the honeycomb YSZ scaffold. Reproduced with permission of Ref. [4], copyright 2022 John Wiley and Sons.

stability at 2.0 $A \cdot cm^{-2}$ and 800 °C which was prepared by freeze casting and infiltration method [4]. The SEM and transmission electron microscopic (TEM) images (Fig. 8) revealed that the YSZ scaffold exhibited an extremely low tortuosity factor and high porosity, and the LSC anode was successfully infiltrated onto the surface of the scaffold. The micro/nanohoneycomb structure could effectively improve oxygen ion transport and oxygen molecule diffusion, which remarkably accelerated the OER kinetics. Shao et al. designed a dendritic channel structure LSF-GDC and showed better performance and the improvement in the stability of the anode compared with the sponge-like pore structure due to the acceleration of the oxygen release [88]. Recently, Yu et al. proposed a novel strategy to construct LSC nano-layer with a vertically aligned micro channel anode scaffold and achieved an ultra-high current density of 5.96 $A \cdot cm^{-2}$ at 1.3 V and 800 °C. The micro/nano channel anode design can effectively enhance the SOEC electrochemical performance due to the promotion of the oxygen species generation and release process [100].

5. Conclusions and outlooks

Overall, this review summarizes the latest research progress of SOEC anode materials including single perovskite, double perovskite, RP phase, and spinel oxides, and then introduces various strategies for anode optimization such as combining with ionic conductor, infiltrating OER active species, and structural optimizing. Although great strides have been made toward the development of anode materials, there are still several challenges such as poor stability, unsatisfactory performance and electrode degradation. Designing active and stable anode materials is critical for CO_2 and/or H_2O electrolysis in SOEC. To fabricate high-performance SOEC for the industrial production, some strategies are proposed as follows: (1) Utilizing *in situ* spectroscopic and microscopic characterizations, and electrochemical characterizations to monitor the elementary reactions and the degradation processes of the SOEC anode during long-term operation, which can offer instructive suggestions for preparing advanced anode materials. (2) Incorporating the selective oxidation of light alkanes at the anode, which can promote electroreduction reaction at a cathode and simultaneously convert light alkanes to valuable chemicals using the generated oxygen species at an anode. (3) With the help of machine learning to predict the physicochemical properties (e.g., ionic conductivity, electronic conductivity, oxygen vacancy concentration, oxygen ion mobility, electronegativity) and implement high-throughput screening and design for advanced anode materials.

Declaration of competing interest

The authors declare no conflict of interest.

Acknowledgements

We gratefully acknowledge financial support from the National Key R&D Program of China (2021YFA1502400), the National Natural Science Foundation of China (22002166, 22125205), Strategic Priority Research Program of the Chinese Academy of Sciences (XDA21070613), Dalian National Laboratory for Clean Energy (DNL202007, DNL201923). G.X. Wang thanks the financial support from CAS Youth Innovation Promotion (Y201938). We also acknowledge the Photon Science Center for Carbon Neutrality.

References

[1] Sussmann R, Rettinger M. Can we measure a COVID-19-related slowdown in atmospheric CO_2 growth? sensitivity of total carbon column observations[J]. Rem. Sens., 2020, 12(15): 2387.
[2] Song Y F, Zhang X M, Xie K, Wang G X, Bao X H. High-temperature CO_2 electrolysis in solid oxide electrolysis cells: developments, challenges, and prospects[J]. Adv. Mater., 2019, 31(50): 1902033.
[3] Song Y F, Zhang X M, Zhou Y J, Lü H F, Liu Q X, Feng W C, Wang G X, Bao X H. Improving the performance of solid oxide electrolysis cell with gold nanoparticles-modified LSM-YSZ anode[J]. J. Energy Chem., 2019, 35: 181−187.
[4] Wu T, Zhang W Q, Li Y F, Zheng Y, Yu B, Chen J, Sun X M. Micro-/nanohoneycomb solid oxide electrolysis cell anodes with ultralarge current tolerance[J]. Adv. Energy Mater., 2018, 8(33): 1802203.
[5] Fleig J. Solid oxide fuel cell cathodes: polarization mechanisms and modeling of the electrochemical performance [J]. Annu. Rev. Mater. Res., 2003, 33: 361−382.
[6] Shirai Y, Hashimoto S, Sato K, Yashiro K, Amezawa K, Mizusaki J, Kawada T. Crystal structure and thermal expansion behavior of oxygen stoichiometric lanthanum strontium manganite at high temperature[J]. Solid State Ionics, 2014, 256: 83−88.
[7] Shen M H, Ai F J, Ma H L, Xu H, Zhang Y Y. Progress and prospects of reversible solid oxide fuel cell materials[J]. iScience, 2021, 24(12): 103464.
[8] Mikkelsen L, Skou E. Determination of the oxygen chemical diffusion coefficient in perovskites by a thermogravimetric method[J]. J. Therm. Anal. Calorim., 2001, 64(3): 873−878.
[9] Ebbesen S D, Mogensen M. Electrolysis of carbon dioxide in solid oxide electrolysis cells[J]. J. Power Sources, 2009, 193(1): 349−358.
[10] Steele B CH, Hori K M, Uchino S. Kinetic parameters influencing the performance of IT-SOFC composite electrodes[J]. Solid State Ionics, 2000, 135(1): 445−450.
[11] Chen K F, Jiang S P. Failure mechanism of (La,Sr)MnO_3 oxygen electrodes of solid oxide electrolysis cells[J]. Int. J. Hydrogen Energy, 2011, 36(17): 10541−10549.

[12] Knibbe R, Traulsen M L, Hauch A, Ebbesen S D, Mogensen M. Solid oxide electrolysis cells: degradation at high current densities[J]. J. Electrochem. Soc., 2010, 157(8): B1209−B1217.

[13] Mahata A, Datta P, Basu R N. Synthesis and characterization of Ca doped $LaMnO_3$ as potential anode material for solid oxide electrolysis cells[J]. Ceram. Int., 2017, 43(1): 433−438.

[14] Fang Q P, Menzler N H, Blum L. Degradation analysis of long-term solid oxide fuel cell stacks with respect to chromium poisoning in $La_{0.58}Sr_{0.4}Co_{0.2}Fe_{0.8}O_{3-\delta}$ and $La_{0.6}Sr_{0.4}CoO_{3-\delta}$ cathodes[J]. J. Electrochem. Soc., 2021, 168(10): 104505.

[15] Develos Bagarinao K, De Vero J, Kishimoto H, Ishiyama T, Yamaji K, Horita T, Yokokawa H. Multilayered LSC and GDC: an approach for designing cathode materials with superior oxygen exchange properties for solid oxide fuel cells[J]. Nano Energy, 2018, 52: 369−380.

[16] Zheng Y F, Li Q S, Chen T, Wu W, Xu C, Wang W G. Comparison of performance and degradation of large-scale solid oxide electrolysis cells in stack with different composite air electrodes[J]. Int. J. Hydrogen Energy, 2015, 40(6): 2460−2472.

[17] Sharma V I, Yildiz B. Degradation mechanism in $La_{0.8}Sr_{0.2}CoO_3$ as contact layer on the solid oxide electrolysis cell anode[J]. J. Electrochem. Soc., 2010, 157(3): B441−B448.

[18] Zheng H Y, Tian Y F, Zhang L L, Chi B, Pu J, Jian L. $La_{0.8}Sr_{0.2}Co_{0.8}Ni_{0.2}o_{3-\delta}$ impregnated oxygen electrode for H_2O/CO_2 co-electrolysis in solid oxide electrolysis cells[J]. J. Power Sources, 2018, 383: 93−101.

[19] Tan Y, Duan N Q, Wang A, Yan D, Chi B, Wang N, Pu J, Li J. Performance enhancement of solution impregnated nanostructured $La_{0.8}Sr_{0.2}Co_{0.8}Ni_{0.2}O_{3-\delta}$ oxygen electrode for intermediate temperature solid oxide electrolysis cells [J]. J. Power Sources, 2016, 305: 168−174.

[20] Chrzan A, Ovtar S, Jasinski P, Chen M, Hauch A. High performance $LaNi_{1-x}Co_xO_{3-\delta}$($x$=0.4 to 0.7) infiltrated oxygen electrodes for reversible solid oxide cells[J]. J. Power Sources, 2017, 353: 67−76.

[21] Duan N Q, Yang J J, Gao M R, Zhang B W, Luo J L, Du Y H, Xu M H, Jia L C, Chi B, Li J. Multi-functionalities enabled fivefold applications of $LaCo_{0.6}Ni_{0.4}O_{3-\delta}$ in intermediate temperature symmetrical solid oxide fuel/electrolysis cells[J]. Nano Energy, 2020, 77: 105207.

[22] Ma Q L, Dierickx S, Vibhu V, Sebold D, de Haart L GJ, Weber A, Guillon O, Menzler N H. Performances of solid oxide cells with $La_{0.97}Ni_{0.5}Co_{0.5}O_{3-\delta}$ as air-electrodes[J]. J. Electrochem. Soc., 2020, 167(8): 084522.

[23] Khan M S, Xu X Y, Li M R, Rehman A U, Knibbe R, Yago A J, Zhu Z H. Evaluation of $SrCo_{0.8}Nb_{0.2}O_{3-\delta}$, $SrCo_{0.8}Ta_{0.2}O_{3-\delta}$ and $SrCo_{0.8}Nb_{0.1}Ta_{0.1}O_{3-\delta}$ as air electrode materials for solid oxide electrolysis and reversible solid oxide cells[J]. Electrochim. Acta, 2019, 321: 134654.

[24] Patrakeev M V, Bahteeva J A, Mitberg E B, Leonidov I A, Kozhevnikov V L, Poeppelmeier K R. Electron/hole and ion transport in $La_{1-x}Sr_xFeo_{3-\delta}$[J]. J. Solid State Chem., 2003, 172(1): 219−231.

[25] Niu Y J, Sunarso J, Liang F L, Zhou W, Zhu Z H, Shao Z P. A comparative study of oxygen reduction reaction on Bi- and La-doped $SrFeO_{3-\delta}$ perovskite cathodes[J]. J. Electrochem. Soc., 2011, 158(2): B132−B138.

[26] Chavan S V, Singh R N. Preparation, properties, and reactivity of lanthanum strontium ferrite as an intermediate temperature SOFC cathode[J]. J. Mater. Sci., 2013, 48(19): 6597−6604.

[27] Fan H, Zhang Y L, Han M F. Infiltration of $La_{0.6}Sr_{0.4}FeO_{3-\delta}$ nanoparticles into YSZ scaffold for solid oxide fuel cell and solid oxide electrolysis cell[J]. J. Alloys Compd., 2017, 723: 620−626.

[28] Guan C Z, Wang Y D, Chen K F, Xiao G P, Lin X, Zhou J, Song S Z, Wang J Q, Zhu Z Y, Zhou X D. Molten salt synthesis of Nb-doped (La, Sr)FeO_3 as the oxygen electrode for reversible solid oxide cells[J]. Mater. Lett., 2019, 245: 114−117.

[29] Cui C S, Wang Y, Tong Y C, Wang S W, Chen C S, Zhan Z L. Syngas production through CH_4-assisted co-electrolysis of H_2O and CO_2 in $La_{0.8}Sr_{0.2}Cr_{0.5}Fe_{0.5}O_{3-\delta}$-$Zr_{0.84}Y_{0.16}O_{2-\delta}$ electrode-supported solid oxide electrolysis cells[J]. Int. J. Hydrogen Energy, 2021, 46(39): 20305−20312.

[30] Tian Y F, Zheng H Y, Zhang L L, Chi B, Pu J, Li J. Direct electrolysis of CO_2 in symmetrical solid oxide electrolysis cell based on $La_{0.6}Sr_{0.4}Fe_{0.8}Ni_{0.2}O_{3-\delta}$ electrode[J]. J. Electrochem. Soc., 2018, 165(2): F17−F23.

[31] Zhang L J, Li Y H, Zhang B Z, Wan Y H, Xu Z Q, Zhang S W, Zhu T L, Xia C R, La Sr. (Ti,Fe)$O_{3-\delta}$ perovskite with *in-situ* constructed $FeNi_3$ nanoparticles as fuel electrode for reversible solid oxide cell[J]. Int. J. Energy Res., 2021, 45(15): 21264−21273.

[32] Peng X Z, Tian Y F, Liu Y, Wang W J, Jia L C, Pu J, Chi B, Li J. An efficient symmetrical solid oxide electrolysis cell with LSFM-based electrodes for direct electrolysis of pure CO_2[J]. J. CO_2 Util., 2020, 36: 18−24.

[33] Tian Y F, Wang W J, Liu Y, Zhang L L, Jia L C, Yang J, Chi B, Pu J, Li J. Cobalt-free perovskite oxide $La_{0.6}Sr_{0.4}Fe_{0.8}Ni_{0.2}O_{3-\delta}$ as active and robust oxygen electrode for reversible solid oxide cells[J]. ACS Appl. Energy Mater., 2019, 2(5): 3297−3305.

[34] Zheng Y F, Wang S, Pan Z H, Yin B. Electrochemical CO_2 reduction to Co using solid oxide electrolysis cells with high-performance Ta-doped bismuth strontium ferrite air electrode[J]. Energy, 2021, 228: 120579.

[35] Berger C, Bucher E, Gspan C, Sitte W. Crystal structure, oxygen nonstoichiometry, and mass and charge transport properties of the Sr-free SOFC/SOEC air electrode material $La_{0.75}Ca_{0.25}FeO_{3-\delta}$[J]. J. Solid State Chem., 2019, 273: 92−100.

[36] Tian Y F, Zhang L L, Liu Y, Jia L C, Yang J, Chi B, Pu J, Li J. A self-recovering robust electrode for highly efficient CO_2 electrolysis in symmetrical solid oxide electrolysis cells[J]. J. Mater Chem., 2019, 7(11): 6395−6400.

[37] Tan T, Wang Z M, Qin M X, Zhong W T, Hu J H, Yang C H, Liu M L. *In situ* exsolution of core-shell structured NiFe/FeO_x nanoparticles on $Pr_{0.4}Sr_{1.6}(NiFe)_{1.5}Mo_{0.5}O_{6-\delta}$ for CO_2 electrolysis[J]. Adv. Funct. Mater., 2022, 32(34): 2202878.

[38] Zhang L H, Xu C M, Sun W, Ren R Z, Yang X X, Luo Y Z, Qiao J S, Wang Z H, Zhen S Y, Sun K N. Constructing perovskite/alkaline-earth metal composite heterostructure by infiltration to revitalize CO_2 electrolysis[J]. Sep. Purif. Technol., 2022, 298: 121475.

[39] Simrick N J, Kilner J A, Atkinson A, Rupp J LM, Ryll T M, Bieberle-Hütter A, Galinski H, Gauckler L J. Microfabrication of patterned LSCF thin-film cathodes with gold current collectors[J]. Solid State Ionics, 2011, 192(1): 619−626.

[40] Jiang S P. A comparison of O_2 reduction reactions on porous (La,Sr)MnO_3 and (La,Sr)(Co,Fe)O_3 electrodes[J]. Solid State Ionics, 2002, 146(1): 1−22.

[41] Laguna-Bercero M A, Kilner J A, Skinner S J. Development of oxygen electrodes for reversible solid oxide fuel cells with scandia stabilized zirconia electrolytes[J]. Solid State Ionics, 2011, 192(1): 501−504.

[42] Lei C, Simpson M F, Virkar A V. Investigation of ion and electron conduction in the mixed ionic-electronic

conductor-La-Sr-Co-Fe-oxide (LSCF) using alternating current (ac) and direct current (dc) techniques[J]. J. Electrochem. Soc., 2022, 169(1): 014506.

[43] Tai L W, Nasrallah M M, Anderson H U, Sparlin D M, Sehlin S R. Structure and electrical properties of $La_{1-x}Sr_xCo_{1-y}Fe_yO_3$. Part 2. The system $La_{1-x}Sr_xCo_{0.2}Fe_{0.8}O_3$[J]. Solid State Ionics, 1995, 76(3): 273−283.

[44] Ai N, He S, Li N, Zhang Q, Rickard W DA, Chen K F, Zhang T, Jiang S P. Suppressed Sr segregation and performance of directly assembled $La_{0.6}Sr_{0.4}Co_{0.2}Fe_{0.8}O_{3-\delta}$ oxygen electrode on Y_2O_3-ZrO_2 electrolyte of solid oxide electrolysis cells[J]. J. Power Sources, 2018, 384: 125−135.

[45] Yang Z B, Wang N, Ma C Y, Jin X F, Lei Z, Xiong X Y, Peng S P. Co-electrolysis of H_2O-CO_2 in a solid oxide electrolysis cell with symmetrical $La_{0.4}Sr_{0.6}Co_{0.2}Fe_{0.7}Nb_{0.1}O_{3-\delta}$ electrode[J]. J. Electroanal. Chem., 2019, 836: 107−111.

[46] Shao Z P, Yang W S, Cong Y, Dong H, Tong J H, Xiong G X. Investigation of the permeation behavior and stability of a $Ba_{0.5}Sr_{0.5}Co_{0.8}Fe_{0.2}O_{3-\delta}$ oxygen membrane[J]. J. Membr Sci., 2000, 172(1−2): 177−188.

[47] Liang F Y, Jiang H Q, Luo H X, Kriegel R, Caro J. High-purity oxygen production by a dead-end $Ba_{0.5}Sr_{0.5}Co_{0.8}Fe_{0.2}O_{3-\delta}$ tube membrane[J]. Catal. Today, 2012, 193(1): 95−100.

[48] Shiiba H, Bishop C L, Rushton M JD, Nakayama M, Nogami M, Kilner J A, Grimes R W. Effect of a-site cation disorder on oxygen diffusion in perovskite-type $Ba_{0.5}Sr_{0.5}Co_{1-x}Fe_xO_{2.5}$[J]. J. Mater Chem., 2013, 1(35): 10345−10352.

[49] Wang L, Merkle R, Maier J. Oxygen reduction kinetics and transport properties of $(Ba,Sr)(Co,Fe)O_{3-\delta}$ and related SOFC cathode materials[J]. ECS Trans., 2009, 25(2): 2497−2505.

[50] Yu B, Zhang W Q, Xu J M, Chen J. Microstructural characterization and electrochemical properties of $Ba_{0.5}Sr_{0.5}Co_{0.8}Fe_{0.2}O_{3-\delta}$ and its application for anode of SOEC[J]. Int. J. Hydrogen Energy, 2008, 33(23): 6873−6877.

[51] Wang H H, Cong Y, Yang W S. Investigation on the partial oxidation of methane to syngas in a tubular $Ba_{0.5}Sr_{0.5}Co_{0.8}Fe_{0.2}O_{3-\delta}$ membrane reactor[J]. Catal. Today, 2003, 82(1): 157−166.

[52] Li M, Hua B, Chen J, Zhong Y M, Luo J L. Charge transfer dynamics in RuO_2/perovskite nanohybrid for enhanced electrocatalysis in solid oxide electrolyzers[J]. Nano Energy, 2019, 57: 186−194.

[53] Prasopchokkul P, Seeharaj P, Kim-Lohsoontorn P. $Ba_{0\cdot5}Sr_{0\cdot5}(Co_{0\cdot8}Fe_{0.2})_{1-x}Ta_xO_{3-\delta}$ perovskite anode in solid oxide electrolysis cell for hydrogen production from high-temperature steam electrolysis[J]. Int. J. Hydrogen Energy, 2021, 46(10): 7023−7036.

[54] Yang Z B, Jin C, Yang C H, Han M F, Chen F L. $Ba_{0.9}Co_{0.5}Fe_{0.4}Nb_{0.1}O_{3-\delta}$ as novel oxygen electrode for solid oxide electrolysis cells[J]. Int. J. Hydrogen Energy, 2011, 36(18): 11572−11577.

[55] He B B, Zhao L, Song S X, Liu T, Chen F L, Xia C R. $Sr_2Fe_{1.5}Mo_{0.5}O_{6-\delta}$-$Sm_{0.2}Ce_{0.8}O_{1.9}$ composite anodes for intermediate-temperature solid oxide fuel cells[J]. J. Electrochem. Soc., 2012, 159(5): B619−B626.

[56] Zhang S W, Zhu K, Hu X Y, Peng R R, Xia C R. Antimony doping to greatly enhance the electrocatalytic performance of $Sr_2Fe_{1.5}Mo_{0.5}O_{6-\delta}$ perovskite as a ceramic anode for solid oxide fuel cells[J]. J. Mater Chem., 2021, 9(43): 24336−24347.

[57] Liu Q, Yang C H, Dong X H, Chen F L. Perovskite $Sr_2Fe_{1.5}Mo_{0.5}O_{6-\delta}$ as electrode materials for symmetrical solid oxide electrolysis cells[J]. Int. J. Hydrogen Energy, 2010, 35(19): 10039−10044.

[58] Dai N N, Feng J, Wang Z H, Jiang T Z, Sun W, Qiao J S, Sun K N. Synthesis and characterization of B-site Ni-doped perovskites $Sr_2Fe_{1.5-x}Ni_xMo_{0.5}O_{6-\delta}$ (x=0, 0.05, 0.1, 0.2, 0.4) as cathodes for sofcs[J]. J. Mater Chem., 2013, 1(45): 14147−14153.

[59] Yang Y R, Wang Y H, Yang Z B, Chen Y, Peng S P. A highly active and durable electrode with *in situ* exsolved Co nanoparticles for solid oxide electrolysis cells[J]. J. Power Sources, 2020, 478: 229082.

[60] Yang Y, Shi N, Xie Y, Li X Y, Hu X Y, Zhu K, Huan D M, Peng R R, Xia C R, Lu Y L. K doping as a rational method to enhance the sluggish air-electrode reaction kinetics for proton-conducting solid oxide cells[J]. Electrochim. Acta, 2021, 389: 138453.

[61] Wei B, Chen K, Zhao L, Ai N, Lü Z, Jiang S P. SmBa-$Co_2O_{5+\delta}$ as high efficient oxygen electrode of solid oxide electrolysis cells[J]. ECS Trans., 2013, 57(1): 3189−3196.

[62] Zheng Y F, Yang H, Pan Z H, Zhang C Z. A Ca and Fe co-doped layered perovskite as stable air electrode in solid oxide electrolyzer cells under high-current electrolysis[J]. Electrochim. Acta, 2017, 251: 581−587.

[63] Niu B B, Lu C L, Yi W D, Luo S J, Li X N, Zhong X W, Zhao X Z, Xu B M. *In-situ* growth of nanoparticles-decorated double perovskite electrode materials for symmetrical solid oxide cells[J]. Appl. Catal. B, 2020, 270: 118842.

[64] Jun A, Kim J, Shin J, Kim G. Achieving high efficiency and eliminating degradation in solid oxide electrochemical cells using high oxygen-capacity perovskite[J]. Angew. Chem. Int. Ed., 2016, 55(40): 12512−12515.

[65] Tian Y F, Yan D, Chi B, Chen J, Li X, Li J. Preparation and properties of $PrBa_{0.5}Sr_{0.5}Co_{1.5}Fe_{0.5}O_{5+\delta}$ as novel oxygen electrode for solid oxide electrolysis cells[J]. ECS Trans., 2017, 78(1): 533−541.

[66] Vibhu V, Flura A, Rougier A, Nicollet C, Fourcade S, Hungria T, Grenier J C, Bassat J M. Electrochemical ageing study of mixed lanthanum/praseodymium nickelates $La_{2-x}Pr_xNiO_{4+\delta}$ as oxygen electrodes for solid oxide fuel or electrolysis cells[J]. J. Energy Chem., 2020, 46: 62−70.

[67] Chauveau F, Mougin J, Bassat J M, Mauvy F, Grenier J C. A new anode material for solid oxide electrolyser: the neodymium nickelate $Nd_2NiO_{4+\delta}$[J]. J. Power Sources, 2010, 195(3): 744−749.

[68] Chauveau F, Mougin J, Mauvy F, Bassat J M, Grenier J C. Electrochemical performances of cells containing alternative oxygen electrodes, $Ln_2NiO_{4+\delta}$ (Ln=Nd, La)[J]. ECS Trans., 2009, 25(2): 2557−2564.

[69] Kim S J, Kim K J, Dayaghi A M, Choi G M. Polarization and stability of $La_2NiO_{4+\delta}$ in comparison with $La_{0.6}Sr_{0.4}Co_{0.2}Fe_{0.8}O_{3-\delta}$ as air electrode of solid oxide electrolysis cell[J]. Int. J. Hydrogen Energy, 2016, 41(33): 14498−14506.

[70] Vibhu V, Vinke I C, Eichel R A, Bassat J M, de Haart L GJ. $La_2Ni_{1-x}CoO_{4+\delta}$ (x=0.0, 0.1 and 0.2) based efficient oxygen electrode materials for solid oxide electrolysis cells[J]. J. Power Sources, 2019, 444: 227292.

[71] Laguna-Bercero M A, Kinadjan N, Sayers R, El Shinawi H, Greaves C, Skinner S J. Performance of $La_{2-x}Sr_xCo_{0.5}Ni_{0.5}O_{4\pm\delta}$ as an oxygen electrode for solid oxide reversible cells[J]. Fuel Cell, 2011, 11(1): 102−107.

[72] Ogier T, Mauvy F, Bassat J M, Laurencin J, Mougin J, Grenier J C. Overstoichiometric oxides $Ln_2NiO_{4+\delta}$ (Ln=La, Pr or Nd) as oxygen anodic electrodes for solid oxide electrolysis application[J]. Int. J. Hydrogen Energy, 2015, 40(46): 15885−15892.

[73] Vibhu V, Vinke I C, Eichel R A, de Haart L GJ. Cobalt substituted $Pr_2Ni_{1-x}CoO_{4+\delta}$ (x=0, 0.1, 0.2) oxygen electrodes: impact on electrochemical performance and

durability of solid oxide electrolysis cells[J]. J. Power Sources, 2021, 482: 228909.

[74] Huan D M, Zhang L, Zhang S W, Shi N, Li X Y, Zhu K, Xia C R, Peng R R, Lu Y L. Ruddlesden-popper oxide $SrEu_2Fe_2O_7$ as a promising symmetrical electrode for pure CO_2 electrolysis[J]. J. Mater Chem., 2021, 9(5): 2706−2713.

[75] Zheng Y F, Jiang H G, Wang S, Qian B, Li Q S, Ge L, Chen H. Mn-doped ruddlesden-popper oxide $La_{1.5}Sr_{0.5}NiO_{4+\delta}$ as a novel air electrode material for solid oxide electrolysis cells[J]. Ceram. Int., 2021, 47(1): 1208−1217.

[76] Liu S M, Zhang W Q, Li Y F, Yu B. $ReBaCO_2O_{5+\delta}$ (Re = Pr, Nd, and Gd) as promising oxygen electrodes for intermediate-temperature solid oxide electrolysis cells[J]. RSC Advances, 2017, 7(27): 16332−16340.

[77] Zhou Q J, He T M, Ji Y. $SmBaCo_2O_{5+x}$ double-perovskite structure cathode material for intermediate-temperature solid-oxide fuel cells[J]. J. Power Sources, 2008, 185(2): 754−758.

[78] Sun C Z, Kong Y, Shao L, Zhang Q, Wu X, Zhang N Q, Sun K N. Significant zirconium substitution effect on the oxygen reduction activity of the cathode material $NdBaCo_2O_{5+\delta}$ for solid oxide fuel cells[J]. ACS Sustain. Chem. Eng., 2019, 7(13): 11603−11611.

[79] Du Z H, Li K Y, Zhao H L, Dong X, Zhang Y, Świerczek K. A $SmBaCo_2O_{5+\delta}$ double perovskite with epitaxially grown $Sm_{0.2}Ce_{0.8}O_{2-\delta}$ nanoparticles as a promising cathode for solid oxide fuel cells[J]. J. Mater Chem., 2020, 8(28): 14162−14170.

[80] Zhang L L, Tian Y F, Liu Y T, Jia L C, Yang J, Chi B, Pu J, Li J. Direct electrolysis of CO_2 in a symmetrical solid oxide electrolysis cell with spinel $MnCo_2O_4$ as electrode[J]. Chemelectrochem, 2019, 6(5): 1359−1364.

[81] Duan N Q, Gao M R, Hua B, Li M, Chi B, Li J, Luo J L. Exploring $Ni(Mn_{1/3}Cr_{2/3})_2O_4$ spinel-based electrodes for solid oxide cells[J]. J. Mater Chem., 2020, 8(7): 3988−3998.

[82] Kim D, Thaheem I, Yu H, Park J H, Lee K T. Highly promoted electrocatalytic activity of spinel $CoFe_2O_4$ by combining with $Er_{0.4}Bi_{1.6}O_3$ as a bifunctional oxygen electrode for reversible solid oxide cells[J]. J. Mater Chem., 2022, 10(4): 2045−2054.

[83] Zhao Q, Yan Z H, Chen C C, Chen J. Spinels: controlled preparation, oxygen reduction/evolution reaction application, and beyond[J]. Chem. Rev., 2017, 117(15): 10121−10211.

[84] Yang C H, Jin C, Coffin A, Chen F L. Characterization of infiltrated $(La_{0.75}Sr_{0.25})_{0.95}MnO_3$ as oxygen electrode for solid oxide electrolysis cells[J]. Int. J. Hydrogen Energy, 2010, 35(11): 5187−5193.

[85] Song Y F, Zhang X M, Zhou Y J, Jiang Q K, Guan F, Lv H F, Wang G X, Bao X H. Promoting oxygen evolution reaction by RuO_2 nanoparticles in solid oxide CO_2 electrolyzer[J]. Energy Stor. Mater., 2018, 13: 207−214.

[86] Zhang S L, Wang H Q, Lu M Y, Li C X, Li C J, Barnett S A. Electrochemical performance and stability of $SrTi_{0.3}Fe_{0.6}Co_{0.1}O_{3-\delta}$ infiltrated $La_{0.8}Sr_{0.2}MnO_3$-$Zr_{0.92}Y_{0.16}O_{2-\delta}$ oxygen electrodes for intermediate-temperature solid oxide electrochemical cells[J]. J. Power Sources, 2019, 426: 233−241.

[87] Yun B H, Kim K J, Joh D W, Chae M S, Lee J J, Kim D W, Kang S, Choi D, Hong S T, Lee K T. Highly active and durable double-doped bismuth oxide-based oxygen electrodes for reversible solid oxide cells at reduced temperatures[J]. J. Mater Chem., 2019, 7(36): 20558−20566.

[88] Li T P, Wang T P, Wei T, Hu X, Ye Z M, Wang Z, Dong D H, Chen B, Wang H T, Shao Z P. Robust anode-supported cells with fast oxygen release channels for efficient and stable CO_2 electrolysis at ultrahigh current densities[J]. Small, 2021, 17(6): 2007211.

[89] Wang Y, Xu J H, Meng X Y, Liu T, Chen F L. Ni infiltrated $Sr_2Fe_{1.5}Mo_{0.5}O_{6-\delta}$-$Ce_{0.8}Sm_{0.2}O_{1.9}$ electrode for methane assisted steam electrolysis process[J]. Electrochem. Commun., 2017, 79: 63−67.

[90] Liu T, Liu H, Zhang X Y, Lei L, Zhang Y X, Yuan Z H, Chen F L, Wang Y. A robust solid oxide electrolyzer for highly efficient electrochemical reforming of methane and steam[J]. J. Mater Chem., 2019, 7(22): 13550−13558.

[91] Chen K F, Ai N, Jiang S P. Performance and stability of $(La,Sr)MnO_3$-Y_2O_3-ZrO_2 composite oxygen electrodes under solid oxide electrolysis cell operation conditions[J]. Int. J. Hydrogen Energy, 2012, 37(14): 10517−10525.

[92] Liu Y, Tian Y F, Wang W J, Li Y T, Chattopadhyay S, Chi B, Pu J. Promoting electrocatalytic activity and stability via $Er_{0.4}Bi_{1.6}O_{3-\delta}$ *in situ* decorated $La_{0.8}Sr_{0.2}MnO_{3-\delta}$ oxygen electrode in reversible solid oxide cell[J]. ACS Appl. Mater. Interfaces., 2020, 12(52): 57941−57949.

[93] Chen K F, Ai N, Jiang S P. Development of $(Gd,Ce)O_2$-impregnated $(La,Sr)MnO_3$ anodes of high temperature solid oxide electrolysis cells[J]. J. Electrochem. Soc., 2010, 157(11): P89−P94.

[94] Gondolini A, Mercadelli E, Sanson A. Single step anode-supported solid oxide electrolyzer cell[J]. J. Eur. Ceram. Soc., 2015, 35(16): 4617−4621.

[95] Chen K F, Ai N, Jiang S P. Enhanced electrochemical performance and stability of $(La,Sr)MnO_3$-$(Gd,Ce)O_2$ oxygen electrodes of solid oxide electrolysis cells by palladium infiltration[J]. Int. J. Hydrogen Energy, 2012, 37(2): 1301−1310.

[96] Tan Y, Gao S, Xiong C Y, Chi B. Nano-structured LSM-YSZ refined with PdO/ZrO_2 oxygen electrode for intermediate temperature reversible solid oxide cells[J]. Int. J. Hydrogen Energy, 2020, 45(38): 19823−19830.

[97] Men H J, Tian N, Qu Y M, Wang M, Zhao S, Yu J. Improved performance of a lanthanum strontium manganite-based oxygen electrode for an intermediate-temperature solid oxide electrolysis cell realized via ionic conduction enhancement[J]. Ceram. Int., 2019, 45(6): 7945−7949.

[98] Khoshkalam M, Đ Tripković, Tong X F, Faghihi-Sani M A, Chen M, Hendriksen P V. Improving oxygen incorporation rate on $(La_{0.6}Sr_{0.4})_{0.98}FeO_{3-\delta}$ via $Pr_2Ni_{1-x}Cu_xO_{4+\delta}$ surface decoration[J]. J. Power Sources, 2020, 457: 228035.

[99] Sar J, Charlot F, Almeida A, Dessemond L, Djurado E. Coral microstructure of graded CGO/LSCF oxygen electrode by electrostatic spray deposition for energy (IT-SOFC, SOEC)[J]. Fuel Cell, 2014, 14(3): 357−363.

[100] Cao J W, Li Y F, Zheng Y, Wang S B, Zhang W Q, Qin X F, Geng G, Yu B. A novel solid oxide electrolysis cell with mmicro-/nano channel anode for electrolysis at ultra-high current density over 5 A cm^{-2}[J]. Adv. Energy Mater. 2022: 2200899.

固体氧化物电解池阳极材料研究进展

邹　庚 [a,b]，冯炜程 [a,b]，宋月锋 [a,*]，汪国雄 [a,*]
[a] 中国科学院大连化学物理研究所，催化国家重点实验室，洁净能源国家实验室，辽宁 大连 116023
[b] 中国科学院大学，北京 100049

摘要

近年来，固体氧化物电解池（SOEC）作为一种高效的电化学能量转换装置，由于其大电流密度、高法拉第效率和高能量效率受到广泛的关注。阳极析氧反应（OER）是 SOEC 中重要的电极反应，涉及四电子转移过程，反应动力学缓慢，在电解过程中阳极极化电阻较大且能耗高。因此，设计高效稳定的阳极材料对提高 SOEC 性能及推动 SOEC 实际应用至关重要。近年来，高性能阳极研究取得了一系列进展。在本综述中，重点介绍了 CO_2 和 H_2O 电解的反应机理，总结了不同类型阳极材料的物理化学和电化学性能，讨论了各种有效的阳极优化策略。此外，还对 SOEC 的未来研究进行了展望。这对阳极材料的发展和 SOEC 的实际应用有一定的指导意义。

关键词：固体氧化物电解池；阳极材料；CO_2 和/或 H_2O 电解；钙钛矿氧化物